Radiotherapy and Oncology 159 (2021) 224–230

Contents lists available at ScienceDirect

Radiotherapy and Oncology

journal homepage: www.thegreenjournal.com

Original Article

Thermoacoustic range verification during pencil beam delivery of a clinical plan to an abdominal imaging phantom

Sarah K. Patch [a,g,*], Chinh Nguyen [a], Diego Dominguez-Ramirez [a], Rudi Labarbe [b], Guillaume Janssens [b], Diego Cammarano [b], Jake Lister [b], Christopher Finch [b], Jamil Lambert [c], Jeevan Pandey [c], Christopher Bennett [c], Elizabeth Porteous [c], Cezarina Chirvase [d], Marie Cohilis [e], Kevin Souris [e], Shigeto Ono [f], Ted Lynch [f]

[a] University of Wisconsin – Milwaukee, United States; [b] Ion Beam Applications, Belgium; [c] Rutherford Cancer Centres; [d] HCA Healthcare, UK; [e] UC Louvain, Belgium; [f] Computerized Imaging Reference Systems; and [g] Acoustic Range Estimates, United States

ARTICLE INFO

Article history:
Received 30 October 2020
Received in revised form 17 March 2021
Accepted 18 March 2021
Available online 30 March 2021

Keywords:
Range verification
Ion therapy
Proton therapy
Thermoacoustic
Ionoacoustic

ABSTRACT

Purpose: The purpose of this phantom study is to demonstrate that thermoacoustic range verification could be performed clinically. Thermoacoustic emissions generated in an anatomical multimodality imaging phantom during delivery of a clinical plan are compared to simulated emissions to estimate range shifts compared to the treatment plan.

Methods: A single-field 12-layer proton pencil beam scanning (PBS) treatment plan created in Pinnacle prescribing 6 Gy/fraction was delivered by a superconducting synchrocyclotron to a triple modality (CT, MRI, and US) abdominal imaging phantom. Data was acquired by four acoustic receivers rigidly affixed to a linear ultrasound array. Receivers 1–2 were located distal to the treatment volume, whereas 3–4 were lateral. Receivers' room coordinates were computed relative to the ultrasound image plane after co-registration to the planning CT volume.

For each prescribed beamlet, a set of thermoacoustic emissions corresponding to varied beam energies were computed. Simulated emissions were compared to measured emissions to estimate shifts of the Bragg peak.

Results: Shifts were small for high-dose beamlets that stopped in soft tissue. Signals acquired by channels 1–2 yielded shifts of -0.2 ± 0.7 mm relative to Monte Carlo simulations for high dose spots (~40 cGy) in the second layer. Additionally, for beam energy ≥125 MeV, thermoacoustic emissions qualitatively tracked lateral motion of pristine beams in a layered gelatin phantom, and time shifts induced by changing phantom layers were self-consistent within nanoseconds.

Conclusions: Acoustic receivers tuned to spectra of thermoacoustic emissions may enable range verification during proton therapy.

 Radiotherapy and Oncology 159 (2021) 224–230

Range uncertainty limits the clinical efficacy and cost effectiveness of proton therapy. Accurate *in vivo* range verification could increase the number of tumor sites for which proton therapy is appropriate. Increasing patient volumes would help justify the added expense of proton therapy. Although the installation cost has dropped from approximately $200 M for a multi-room center to $30 M for a single room facility [1], proton therapy remains expensive compared to conventional X-ray radiation therapy. Additionally, increasing confidence that dose is delivered correctly could justify more hypofractionated protocols, which would reduce overall treatment costs. Currently, concerns about range uncertainty often lead to conservative treatment plans that fail to take full advantage of the Bragg curve and therefore offer limited benefits over x-ray treatment plans.

Because range uncertainty is such a problem, many approaches have been taken to verify range as discussed in the review article by Parodi and Polf [2]. A plethora of simulation and phantom results generated using non-clinical delivery are referenced in the review article by Hickling et al. [3] on thermoacoustic range verification. Acoustic approaches, such as contrast enhanced [4–6] and thermoacoustic range verification are applicable to tumor sites with acoustic paths between the Bragg peak and acoustic hardware. Both acoustic techniques offer online imaging, which can aid in motion management. Thermoacoustic signals are generated in patients during radiotherapy, as deposited energy heats

* Corresponding author at: Acoustic Range Estimates, and the University of Wisconsin – Milwaukee, United States.
E-mail address: Sarah.Patch@AcousticRangeEstimates.com (S.K. Patch).

https://doi.org/10.1016/j.radonc.2021.03.027
0167-8140/

tissue and increases pressure. Therefore, thermoacoustic signal detection is entirely passive, whereas the contrast enhanced approach requires injecting patients with contrast agent before treatment.

Thermoacoustic range verification relies upon depositing dose within a few microseconds to ensure that pressure builds up faster than it propagates away. A fast-extraction synchrotron was used to perform the only clinical study of thermoacoustic range verification [7]. To date, thermoacoustic emissions generated by clinical cyclotrons and synchrocyclotrons have been detected only in research mode [8,9] using off-the-shelf acoustic hardware with sensitivity that exceeded the bandwidth of thermoacoustic emissions.

We present thermoacoustic signals measured by custom receive chains (transducers + amplifiers) tuned to spectra of thermoacoustic emissions. Thermoacoustic emissions were generated by a clinical synchrocyclotron (IBA S2C2) during delivery of 6 Gy by a single field treatment plan to two different phantoms.

Materials

In order to test the performance of a thermoacoustic range verification system, a 12-layer, single field proton pencil beam scanning (PBS) treatment plan was designed in Pinnacle 16.2.1 (Koninklijke Philips N.V.) to deliver 6 Gy per fraction to a 20 mm $\times$ 20 mm field. The nominal spreadout Bragg peak (SOBP) modulation was 57.5 mm. The plan was based upon a 512 $\times$ 512 $\times$ 167 CT volume with 1.19 $\times$ 1.19 $\times$ 1 mm^3 voxel dimensions acquired by a Philips Brilliance Big Bore scanner with the phantom resting directly on the couch. A synchrocyclotron delivered approximately 1–2 cGy (O(10^7) protons) per $4-6\ \mu s$ pulse at a 1 kHz repetition rate. A custom plastic scintillator-photomultiplier tube (PMT) assembly powered by a -2 kV power supply detected gamma emissions. System setup is shown in Fig. 1.

A custom thermoacoustic research system (ARE 4chRev0) consisted of a wireless linear ultrasound array (Clarius L7) with iPad mini display window to which four thermoacoustic receivers were affixed. The thermoacoustic receive chain (transducer + amplifier) was tuned specifically for this application. 10 mm diameter sensors were nearly omnidirectional at 50 kHz, where $\lambda \sim 30mm$. Over 10–100 kHz, transducer receive sensitivity ranged from -25 dB to -30 dB relative to 1 mV/Pa. A dual stage amplifier provided 44–50 dB gain over 10–160 kHz (Supplemental Information D). A four-channel digital oscilloscope enabled remote data acquisition (Siglent SDS1104x-e). The entire assembly could stand upright on a flat surface (Fig. 1b).

Two different gel-based phantoms were used for this study, a commercial, anthropomorphic imaging phantom and a layered gelatin phantom. Lateral and longitudinal beam shifts in the layered phantom are tracked in Supplemental Information sections A and B, respectively. The abdominal phantom (CIRS 057A in Fig. 1c) designed for multimodality imaging was selected because it has clinically relevant and carefully quantified ultrasound, x-ray CT, and MRI properties. Unlike radiotherapy phantoms, soft tissues in this imaging phantom are composed of water-based hydrogels, whereas bone and lung are composed of epoxy resins. Table 1 lists phantom parameters that govern thermoacoustic signal generation and propagation: soundspeed (v_s), density (ρ), volumetric specific heat capacity (C), and volumetric thermal expansion coefficient, (β). The dimensionless Grüneisen parameter, $\Gamma = \beta\rho v_s^2/C$, indicates efficiency with which energy density is converted into pressure and therefore governs amplitude of thermoacoustic signals. Specific heat capacity (C) was measured by an independent lab (Thermtest, Inc.) using the transient plane source method [10]. Representative values for volumetric thermal expansion coefficient (β) were assumed [11]. The most critical parameter for range estimation is soundspeed (v_s), which is inversely proportional to thermoacoustic time of flight. Computerized Imaging Reference Systems (CIRS) quantified density and soundspeed in hydrogels. Soundspeed in air is well-established, and we measured soundspeed in a 5 cm $\times$ 5 cm $\times$ 5 mm bone sample using the substitution technique [12].

Methods

Beam delivery

The treatment plan was delivered layer-by-layer in physics mode. The physics mode enables easy QA and commissioning, and it disables interlocks, warnings, and overrides that protect the patient in clinical mode. The delivered beam is the same as in clinical mode, but physics mode allows the user to restart the irradiation of a field without leaving the irradiation screen and also to deliver the field layer-by-layer. System software tunes and irradiates the beam at each layer as normal, but pauses the beam once after each layer, allowing data to be saved to disc (Fig. 1d).

The thermoacoustic system was supported by a vacbag (MacroMedics Vacuum Cushion) at an oblique angle on the phantom. Receivers 3–4 were not in direct contact with the phantom (Fig. 1e) and a large quantity of coupling gel (Aquasonic) was required to maintain acoustic contact. A CT volume of the evacuated vacbag was acquired subsequently and a region of over 900 pixels had HU values of -916.0 +/$-$ 10.2. The range shifter was inserted to deliver intense beam into the middle of the phantom (Fig. 1f), as degrading upstream reduces proton flux. Receivers 1–2 were positioned higher on the phantom, and distal to the Bragg peaks, whereas 3–4 were lateral (Fig. 1g-h).

Co-registration

To determine thermoacoustic receiver locations, still frame ultrasound images were saved on the iPad mini and later used for co-registration to the volumetric CT. Receiver positions were known relative to the ultrasound array and computed relative to the CT volume as described in Supplemental Information C.

Signal acquisition

Thermoacoustic signals were acquired using the oscilloscope connected to the local area network. Binary files were transferred to a laptop without requiring repeat entry to the treatment room. Channels 1 & 2 recorded thermoacoustic emissions, and channel 3 recorded PMT signal. We refer to the PMT signal as the proton pulse envelope, $I(t)$, which bandlimits thermoacoustic emissions [13]. Channel 4 received the synchrocyclotron's real-time and sequencing electronic unit (SRSEU) trigger which arrived about 480 μs before the PMT signal. Each experiment was repeated, to acquire signals from either thermoacoustic receiver pairs 1–2 or 3–4. Signals were captured layer-by-layer at a 2.5 MSPs readout rate over 2.8 seconds/layer using segmented memory.

Data analysis

Thermoacoustic data analysis was performed offline using MATLAB. System log files provided the order in which spots were painted, number of proton pulses per spot, as well as x-y coordinates and charge recorded on the first ionization chamber (IC) in the proton gantry for each proton pulse. For each layer the entire thermoacoustic time series containing thousands of pulses was low pass filtered below 125 kHz, rather than filtering time series individually. The pulses were then sorted based upon log file

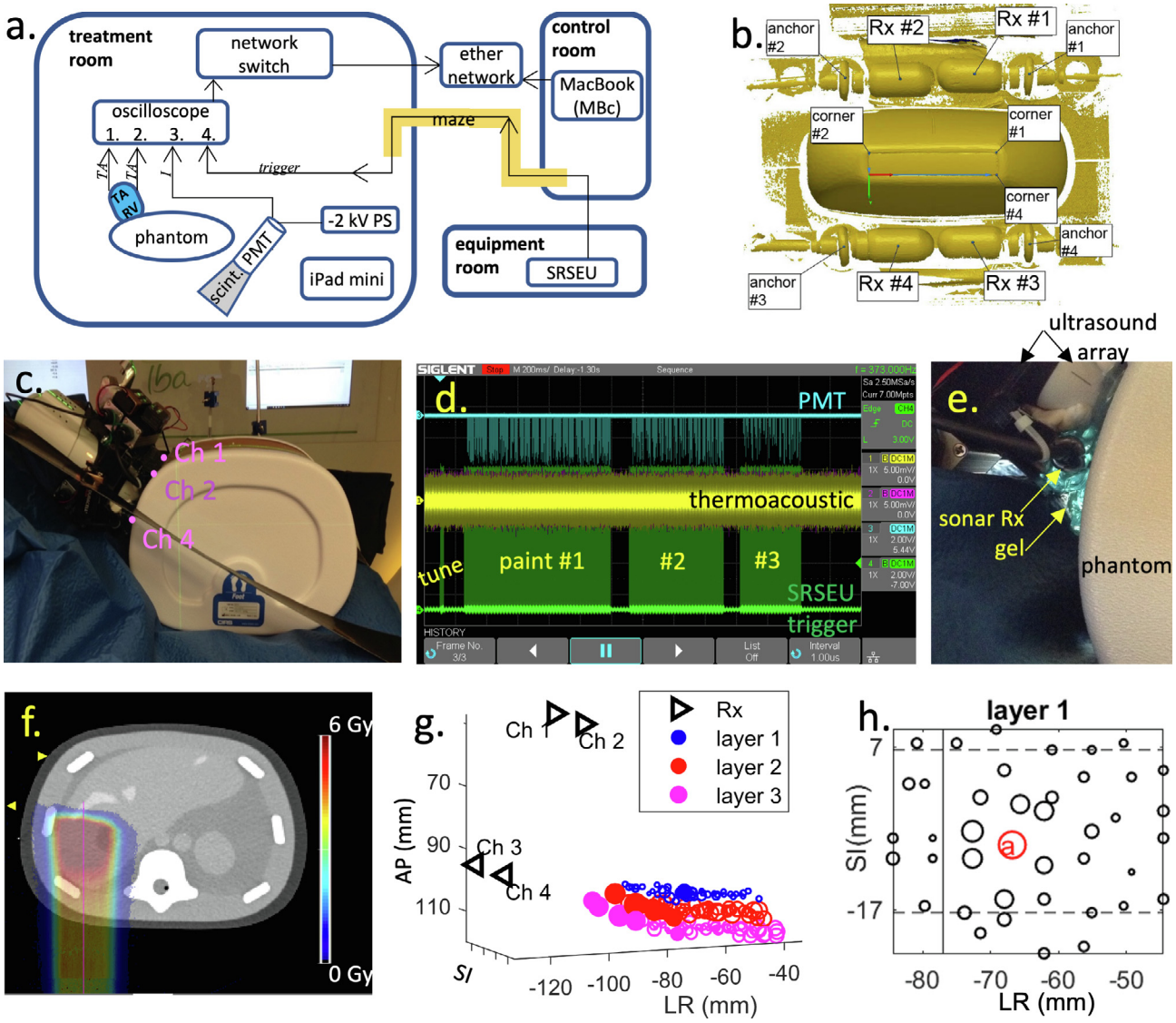

Fig. 1. Experimental setup and data acquisition. a. Experimental layout for testing a 4 channel thermoacoustic range verification prototype. Thermoacoustic range verification (TARV) system is depicted by blue oval. b. Rendered optical scan of the prototype acquired from below. c. A vacbag supported the transducer at an oblique angle. The ultrasound image in Fig. 2d. was acquired in with the transducer in this position. d. Oscilloscope screenshot for layer #3. PMT and SRSEU trigger pulses in cyan and green show tuning pulses and bursts. e. a large volume of acoustic coupling gel was required to maintain acoustic contact between receivers 3 and 4. f. axial slice through isocenter, with total dose overlaid. g. Receivers in black triangles relative to treatment spots. Thermoacoustic emissions from solid spots were analysed (Figs. 2–4). h. Spot map for layer with location of highest dose spot in red. Spot radius is proportional to dose.

Table 1
Properties of the CIRS phantom materials.

	HU range (nominal)	$vs^{\dagger}$(m/s)	$\rho^{\ddagger}$(kg/m^3)	$C^{\ddagger}$(MJ/m^3/K)	β(1/K)	Γ
air	(-5000,-600)	343	1.2	1e-3	3.2e-3	0.45
lung	(-600,-200)	343^	530^	NA^	NA^	NA^
fat	(-200,-25)	1430	894 ± 2.64	1.61±0.07	1.0e-3	1.14
background	(-25, 46)	1540	1040 ± 9.57e-2	3.83±0.44	3.5e-4	0.23
mass	(-25, 46)	1540	1025±1.85e-1	4.69±0.73	3.5e-4	0.18
muscle	(46, 68)	1555	1053 ± 9.66	3.89±0.29	3.5e-4	0.23
liver/kidney/vessel	(68,100)	1540	1084±3.35e-1	4.91±0.96	3.5e-4	0.18
vein	(100,200)	1560	1053±7.04e-1	2.99±0.25	3.5e-4	0.29
bone	(200,Inf)	3200	1313±6.11	1.65±0.04	4.0e-4	3.28
water$^{\#}$	0	1480	1000	NA$^{\#}$	NA$^{\#}$	NA$^{\#}$

‡ μ and σ represent mean and standard deviation, respectively. Mean and standard deviations of densities were computed from 8 measurements, two realizations per each of four samples. Mean and standard deviations of volumetric heat capacity were computed from 5 measurements on a single sample.
† soundspeeds in hydrogels have standard deviation of 5.5 m/s, or 0.35%.
$^{\#}$ in the CT volume used for acoustic simulations a water layer was added to mimic the acoustic coupling gel used during the experiment. The proton beam did not interact with this layer, so thermal properties of water were never used.
^ the proton beam did not interrogate lung, so thermal properties of lung were never used. Density and soundspeed determined the amplitude and phase of acoustic reflections at the lung interface, but reflected signals were not used to estimate range.

information. Weighted averages based upon IC charges were computed for each spot and transducer to yield a total of four thermoacoustic time series and two proton pulse envelopes per treatment spot.

Simulations

Thermoacoustic emissions were modeled by integrating two open-source software packages, OpenReggui (wwww.openreggui.org) and k-Wave (http://www.k-wave.org).

Pinnacle computed the single field dose map analytically, but thermoacoustic range verification requires energy densities for individual beamlets, which were computed using MCsquare [14] Monte Carlo package distributed with OpenReggui [15]. For this study the beam model was generated from commissioning measurements as detailed in Supplemental Information F. We analyzed high dose beamlets in the first three layers with prescribed beam energies of 151.8 MeV, 148.5 MeV, and 145.2 MeV.

To recreate exactly the energy densities delivered, the RT plan was modified in Reggui to include the 40 mm WET range shifter and log files were imported. To account for the vacbag the CT volume was modified by shifting the patient couch downwards by 5.95 mm (5 pixels) and filling the space between the phantom and couch with values of −916 *HU* to mimic the vacbag.

The simulation tracked 10^6 protons per beamlet, and the Bragg peak location for each beamlet was determined from its energy map.

Acoustic simulations performed using k-Wave executed the pseudospectral method [16]. The source term is expressed mathematically as

$$S(\mathbf{x}, t) = E(\mathbf{x})\Gamma(\mathbf{x})\frac{d}{dt}I(t)$$

where $E(\mathbf{x})$ is the energy density deposited per proton pulse in units of J/m^3 as computed by MCsquare, $\Gamma(\mathbf{x})$ is the dimensionless Grüneisen assigned to the segmented CT according to values in Table 1 and $I(t)$ is the PMT measurement, normalized to represent an approximate delta function. Note that energy density is simply dose in Gy times tissue density, $E = \rho D$. The CT volume was zero padded in the SI direction to $512 \times 512 \times 256$ and segmented based upon CT HU values alone. Small "islands" due to noise in the CT reconstruction were removed to improve numerical stability. Soundspeed assignments differentiate fat, muscle, vein and bone from all other soft tissues (Fig. 2).

Range computations for individual beamlets

To overcome the diffraction limit of half wavelength accuracy ($\lambda/2 \sim 15$ mm at 50 kHz) we assumed the lateral (LR and SI) coordinates were correct and applied a simplified version of the 2-step method [17] to signals from receivers 1–2. A set of thermoacoustic emissions was simulated by varying beam energy in 1 MeV increments, with $dE = -4, -3, -2, \cdots, 4\ MeV$. For each energy offset, coordinates of the Bragg peak and time shifts between simulated and measured thermoacoustic signals were computed. Ideally, the measured signal would agree with simulated signal from the planned beamlet. In practice, the measured signal may arrive between simulated emissions from energy-offset beamlets. Linear interpolation between the known Bragg peak locations of the simulated beamlets yielded a shifted Bragg peak location for the delivered beamlet.

Results

Thermoacoustic emissions generated during delivery of RT plan to abdominal phantom are plotted in Figs. 2 and 3. Because $\Gamma_{bone} \gg \Gamma_{soft}$ signal amplitude is greater when beamlets stopped in bone. Beamlets were selected for Figs. 2 and 3 to highlight differences in thermoacoustic emissions generated by beams that stop in soft tissue versus bone. Channels 1–2 were located distal to the Bragg peak and recorded the classic "N-shaped" thermoacoustic emission. Signals recorded by laterally offset channels 3–4 were essentially zero when the acoustic path from the Bragg peak was blocked by a rib bone (Fig. 2), and exhibited ringing due to multiple reflections when the beam hit the bone (Fig. 3). Measured and simulated thermoacoustic emissions are plotted in color with thick and thin lines, respectively. Measured voltages are plotted (thick lines) with 2 millivolt (mV) offsets between channels to improve visibility. Simulated pressures (thin lines) were plotted with the same offsets, and channels 1–2 were rescaled to have the same maximum amplitude as measured signals. Proton pulse envelopes in black confirm pulse durations of $4-6\ \mu s$ full width at half maximum. Axial images through the center of each beamlet represent soundspeed (Fig. 2) and CT image (Fig. 3), with energy density overlaid in color. Axial locations of channels 1 & 2 are represented by ▷, whereas channels 3 & 4 are represented by ◁. Circle radii in the spot maps represent total dose delivered to the spot, which is approximately proportional to the number of proton pulses delivered.

Generally, range shifts are most accurately computed using receiver locations distal to the Bragg peak [18]. Table 2 contains results for beamlets that received at least 20 proton pulses (~0.4 Gy/spot) and subtended small azimuthal angles to receivers 1–2 ($\theta \leq 30^\circ$). No spots in the first layer satisfied both criteria but results from the highest dose spot are included for comparison. Measured signals from the 151.8 MeV beamlet delivered to spot a in layer 1 are compared to simulated signals from beamlets on the same trajectory with energies ranging from 147.8 MeV to 155.8 MeV in Fig. 4a-b. Measured signals arrived earlier than planned, between simulated emissions from beams with energies of 153.8 MeV and 154.8 MeV. Interpolating between the known Bragg peak locations of those simulated beamlets provided shifts relative to the planned beamlets as listed in Table 2.

Initial pressures, p_0, in Table 2 assume instantaneous deposition, rather than the $4-6\ \mu s$ FWHM proton pulse envelopes. Nevertheless, these values are proportional to signal amplitude and $p_0 > 15\ Pa$ indicates the beam interacted with bone. Range estimates are expected to be more accurate for beamlets that interrogated only soft tissue than for beamlets that graze bone [19], and that can be seen in our results. 16 high dose beamlets that interacted with bone corresponded to widely varying time shifts ($-0.3 \pm 5.9\ \mu s$). Seven of them required more than $\pm 4\ MeV$ energy shifts to estimate range. "NA" indicates that measured signal either arrived before or after the simulated emission from a 155.8 MeV or 147.8 MeV beamlet, respectively. However, for six spots in layer 2 that stopped in soft tissue measured signals arrived nearly as planned, with tightly distributed time and range shifts of $0.2 \pm 0.6\ \mu s$ and -0.2 ± 0.7 mm, respectively.

Discussion

Our acoustic receive chain was tuned to thermoacoustic emissions (Fig. 4c-d) and results were encouraging, but there were deficiencies in this study. Most notably, the CT was acquired without the vacbag underneath the phantom. Not only was offline manual co-registration slow, it may have resulted in inaccurate estimates of receiver locations. Amplitudes of simulated signals are suspect due to uncertainty in the Grüneisen values for CIRS' phantom materials, which are within 50% of values estimated for soft human tissues, but more than 200% higher for bone [17]. Therefore, beams that graze bone *in vivo* may generate more useful signal than

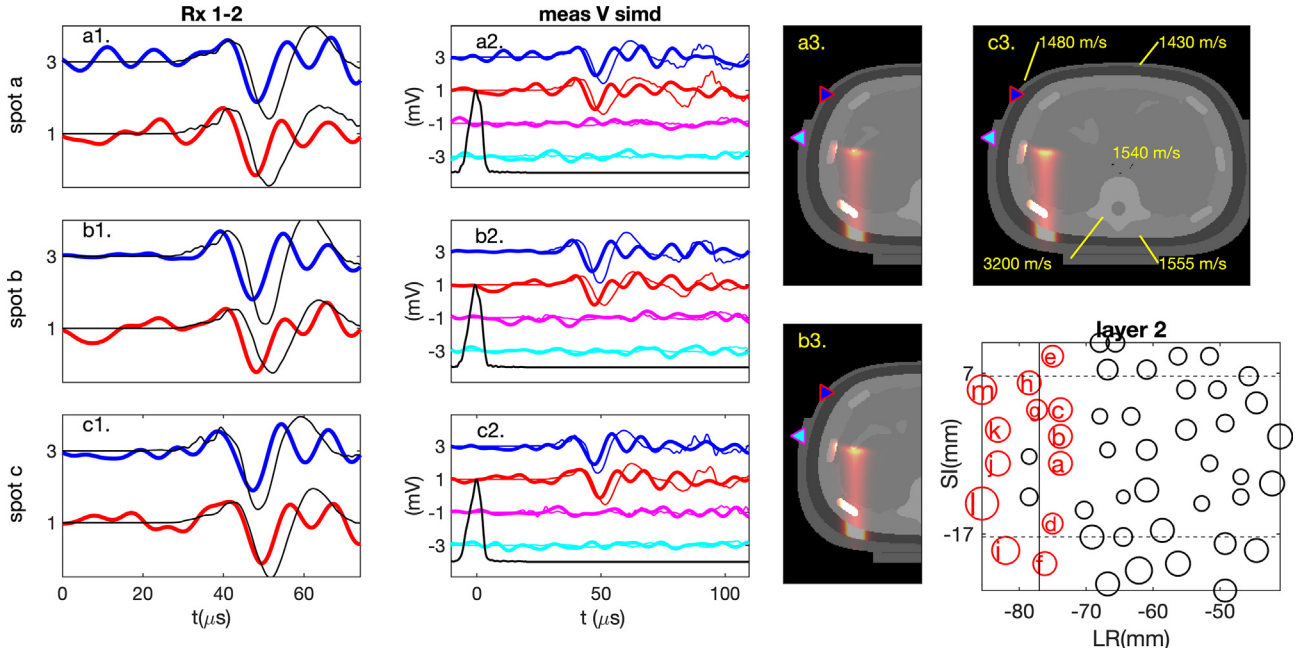

Fig. 2. Layer two results for beamlets a, b, c, that stopped in soft tissue and received 23 proton pulses each (Table 2). Plots of measured and simulated emissions are in thick and thin, respectively, with colors red, blue, magenta and cyan representing channels 1 through 4. Initial pressures are overlaid onto axial images of soundspeed displayed over the window (1300 m/s, 1600 m/s). Soundspeed in a mass visualized by ultrasound is the same as the surrounding liver, but the vein has higher soundspeed. In the spotmap (lower right), lateral locations of treatment spots are indicated by circles. Emissions from red circles have been analysed, and letter labels correspond to thermoacoustic emissions and axial images. Spots left of the vertical black line hit bone. Dashed lines indicate SI locations of receivers.

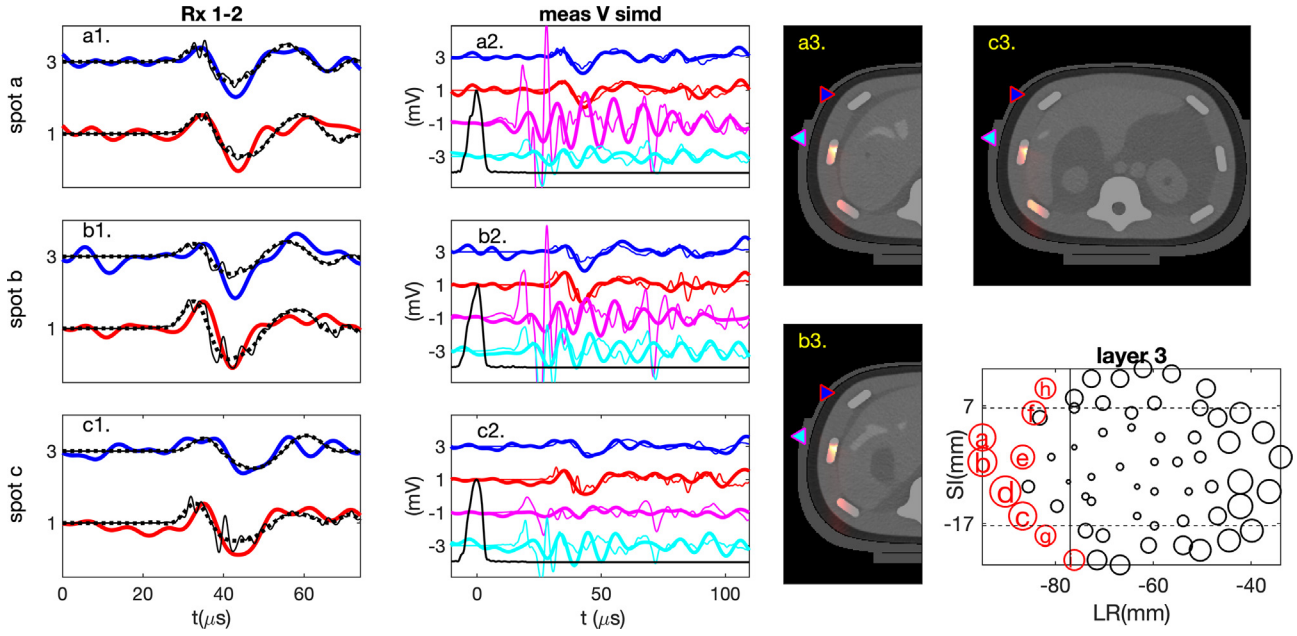

Fig. 3. Layer three results for beamlets a, b, c that hit a rib bone and received 26, 28, and 27 pulses each (Table 2). Initial pressures are overlaid onto CT slices displayed over the HU window (-200, 200). Thick dashed lines represent low-passed simulated data.

obtained in this study. Receivers 3–4 rarely detected useful signals due to their laterally offset locations, leaving only two signals which was insufficient to recover all three coordinates of the Bragg peak. Therefore, lateral beam coordinates were neglected and only range errors were estimated.

Nevertheless, the results were encouraging enough to justify investing engineering effort to make the system more user friendly and robust. For instance, adding channels should ensure at least 3–4 useful signals can be used to estimate lateral coordinates of the Bragg peak as well as range. A custom data acquisition board that enables wireless acquisition of six thermoacoustic channels providing 52 dB amplification is under development (Fig. 4e,g). Modified transducers can provide an additional 3–4 dB sensitivity. A receive chain with greater sensitivity can achieve the same SNR with fewer pulses, so results presented here might be possible for a 2 Gy fraction.

The L7 ultrasound scanner has only a 7 cm imaging depth, and a lower frequency ultrasound array with greater imaging depth

Table 2
Time and range shifts between measured and simulated data compared to initial pressure per proton pulse and cumulative dose within the planned treatment spot, azimuthal angles, and Bragg peak position. Beamlets from layer 2 that stopped in soft tissue in boldface.

	N	$\delta t_1(\mu s)$	$\delta t_2(\mu s)$	δx(mm)	p_0(Pa)	dose (cGy)	θ_1(deg)	θ_2(deg)	LR (mm)	SI (mm)	AP (mm)
1a	21.5	1.5	2.5	−3.4	5.2	34	36	35	−67	−7	105
2a	**23.0**	**1.0**	**0.5**	**−1.0**	**5.0**	**36**	**28**	**28**	**−74**	**−6**	**110**
2b	**23.0**	**−0.2**	**0.6**	**−0.4**	**5.0**	**35**	**27**	**29**	**−74**	**−2**	**110**
2c	**23.0**	**−0.3**	**0.8**	**−0.5**	**5.6**	**37**	**27**	**30**	**−74**	**2**	**110**
2d	**20.0**	**0.4**	**0.0**	**−0.2**	**11.3**	**32**	**31**	**26**	**−75**	**−15**	**110**
2e	**21.0**	**−1.1**	**0.1**	**1.1**	**9.5**	**33**	**26**	**33**	**−75**	**10**	**110**
2f	**23.0**	**0.4**	**−0.2**	**−0.1**	**12.6**	**36**	**33**	**25**	**−76**	**−21**	**110**
2 g	20.0	−4.1	−0.5	NA	16.2	30	25	29	−77	2	109
2 h	23.0	−3.0	−2.3	NA	25.4	37	23	30	−79	6	109
2i	27.0	−0.2	−2.6	3.7	29.8	42	30	21	−82	−19	108
2j	24.0	−1.2	−1.2	3.1	38.6	38	23	22	−83	−6	108
2k	24.0	−1.4	2.3	NA	36.8	36	21	24	−83	−1	108
2l	32.0	−1.1	−0.2	2.3	39.3	51	25	19	−86	−12	107
2m	28.5	−1.7	−1.5	5.4	45.5	43	19	27	−86	5	106
3a	26.0	−0.6	−1.0	2.2	55.9	32	11	19	−95	1	107
3b	28.0	−2.4	−2.0	4.6	60.0	35	14	15	−95	−4	108
3c	27.0	1.0	−1.9	1.6	44.6	39	24	16	−87	−15	112
3d	30.0	−1.9	−1.1	4.6	52.8	45	20	15	−90	−10	110
3e	23.0	−3.7	12.6	NA	44.0	33	18	20	−87	−3	112
3f	23.0	−3.5	−2.0	NA	45.5	34	18	25	−84	6	113
3g	20.0	27.7	−2.2	NA	24.9	30	28	19	−82	−19	114
3h	20.0	−6.0	−3.1	NA	32.4	28	20	29	−82	11	113
3i	20.0	−1.0	1.1	−0.3	16.5	28	32	24	−76	−24	115

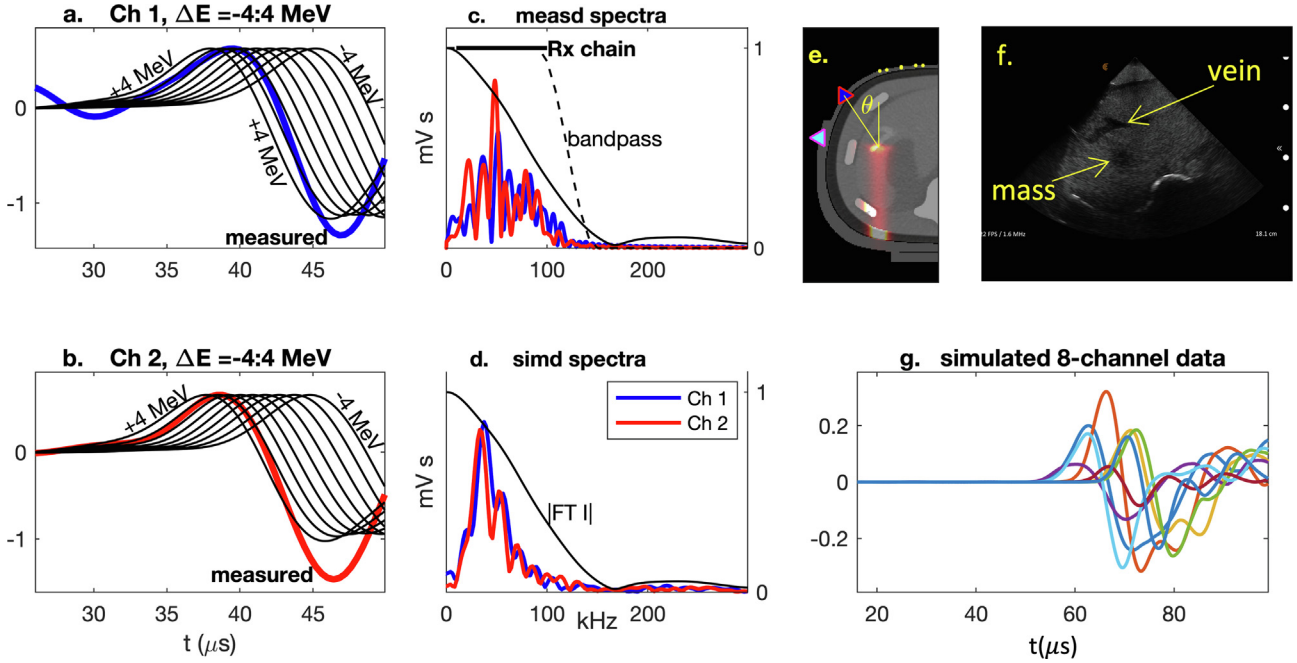

Fig. 4. Results for spot a in layer one. Channel 1–2 measurements in thick blue (a) and red (b), respectively. Simulations for $dE = -4, -3, -2, \cdots, 4$ *MeV* in thin black lines. Spectra of measured (c) and simulated (d) emissions vs amplifier response, $|\boldsymbol{FT}|$,and low-pass kernel in black. e. Axial CT image with highest dose spot overlaid in color, with aziumuthal angle $\theta > 30^{\circ}$ noted. f. Ultrasound image acquired with a low frequency phased array provides 30 cm imaging depth. g. Simulated thermoacoustic emissions corresponding to eight virtual receivers with axial coordinates indicated by yellow dots in e.

(Fig. 4f) will allow for more flexible positioning to ensure unobstructed acoustic paths. Fig. 4e depicts LR-AP receiver locations of an 8-channel system positioned on the patient's abdomen. For some beamlets, the right-most receivers may be obstructed by a rib bone, but all receivers are distal to the Bragg peak. Segmenting based upon both CT HU values and MRI images will better differentiate soft tissues and accurately assign thermoacoustic properties for acoustic propagation software.

A final technical point is that thermoacoustic range estimates can be extremely robust relative to ultrasound images, even in the presence of soundspeed heterogeneity [12]. Ultrasound scanners assume a uniform soundspeed, and images are deformed due to acoustic heterogeneity. When thermoacoustic receivers are packed onto the ultrasound imaging array, acoustic paths are similar so using the same soundspeed to compute thermoacoustic range estimates provides accuracy relative to the ultrasound image.

Further research can begin without access to beamtime. Simulations can be used to determine which tumor sites and beam angles are amenable to thermoacoustic range verification, optimize

thermoacoustic receiver hardware for different accelerator types, and quantify the impact of proton pulse repetition frequency (Supplemental Information D).

Thermoacoustic range verification is a passive technique, so non-interventional patient studies that do not alter the treatment plan or treatment delivery will be low risk. Successful clinical execution will require addition of a skilled sonographer for several reasons. Firstly, accurate co-registration of ultrasound to CT and/or MRI imaging volumes is needed to compute receiver coordinates so high-quality ultrasound images are needed. Additionally, a sonographer can help guide patient selection (and eventually treatment planning) to ensure transducer placement is within the 30° azimuthal cone (Fig. 4e). For appropriate patients, non-interventional studies would not impact patient care, except to add approximately 5 min setup time. Adaptive planning studies would be obvious follow-ups.

Fortunately, independent clinical developments could improve upon the results presented here. Ultrasound "fusion" with CT and MRI is ubiquitous amongst cart-based ultrasound systems. Applying real-time fusion to images acquired by a wireless ultrasound probe is a low-risk engineering task. Additionally, high dose rate protocols, *e.g.* FLASH, that deliver more protons per stress-confined pulse can improve signal-to-noise ratio. Assuming white noise, when full dose is delivered by a single pulse signals are normally distributed according to $\mathcal{N}(\mu,\sigma)$ and $SNR_1 = \mu/\sigma$. Dividing dose amongst N pulses reduces pressure amplitude but leaves noise unchanged according to $\mathcal{N}(\mu/N,\sigma)$. Summing N diminished signals restores amplitude and increases noise, according to $\mathcal{N}\left(\mu,\sqrt{N}\sigma\right)$ with $SNR_N = \mu/\sqrt{N}\sigma = SNR_1/\sqrt{N}$. Therefore, high dose rate delivery in a single pulse could improve SNR by a factor of $\sqrt{20}$ over our results for beamlets that received at least 20 proton pulses.

Disclosure statements

Dr. Patch reports grants from NIH-NCI, during the conduct of the study; is founder of Acoustic Range Estimates, outside the submitted work; In addition, Dr. Patch has patents PCT/US2017/043125 and PCT/US2018/033546 issued.

Mr. Nguyen reports summer stipend from Acoustic Range Estimates, outside the submitted work.

Mr. Dominguez-Ramirez has nothing to disclose.

Dr. Labarbe has nothing to disclose.

Dr. Janssens has nothing to disclose.

Mr. Cammarano has nothing to disclose.

Mr. Lister has nothing to disclose.

Mr. Finch has nothing to disclose.

Dr. Lambert has nothing to disclose.

Mr. Pandey has nothing to disclose.

Ms. Porteous has nothing to disclose.

Dr. Chirvase has nothing to disclose.

Ms. Cohilis reports grants from Fonds National de la Recherche Scientifique (Télévie, grant number 7652619F), during the conduct of the study.

Dr. Souris reports grants from the Walloon region (MECATECH/BIOWIN, grant number 8090), during the conduct of the study; Dr. Souris is in close collaboration with IBA s.a.

Dr. Lynch reports other from CIRS Inc, during the conduct of the study; other from CIRS Inc., outside the submitted work.

Acknowledgements

Partial funding provided by NIH grant #1R43CA243764-01 and in-kind contributions by I.B.A. and the Rutherford Cancer Centres.

Data sharing

Research data and acoustic simulation software are posted to https://data.mendeley.com/datasets/w33vx978rp/1.

Appendix A. Supplementary data

Supplementary data to this article can be found online at https://doi.org/10.1016/j.radonc.2021.03.027.

References

[1] Zietman AL. Too big to fail? The current status of proton therapy in the USA. Clin Oncol (R Coll Radiol) 2018;30:271–3. https://doi.org/10.1016/j.clon.2017.11.002.

[2] Parodi K, Polf JC. In vivo range verification in particle therapy. Med Phys 2018;45:e1036–50. https://doi.org/10.1002/mp.12960.

[3] Hickling S, Xiang L, Jones KC, Parodi K, Assmann W, Avery S, et al. Ionizing radiation-induced acoustics for radiotherapy and diagnostic radiology applications. Med Phys 2018;45:e707–21. https://doi.org/10.1002/mp.12929.

[4] Apfel R. Activatable Infusable Dispersions Containing Drops of a Superheated Liquid for Methods of Therapy and Diagnosis. Published online November 24, 1998.

[5] Patch S. Particle Therapy Aided by Microbubbles and Ultrasound, PCT/US2018/033546. Published online November 22, 2018.

[6] Carlier B, Heymans SV, Nooijens S, Toumia Y, Ingram M, Paradossi G, et al. Proton range verification with ultrasound imaging using injectable radiation sensitive nanodroplets: a feasibility study. Phys Med Biol 2020;65:065013. https://doi.org/10.1088/1361-6560/ab7506.

[7] Hayakawa Y, Tada J, Arai N, Hosono K, Sato M, Wagai T, et al. Acoustic pulse generated in a patient during treatment by pulsed proton radiation beam. Radiat Oncol Invest 1995;3:42–5.

[8] Jones KC, Vander Stappen F, Bawiec CR, Janssens G, Lewin PA, Prieels D, et al. Experimental observation of acoustic emissions generated by a pulsed proton beam from a hospital-based clinical cyclotron. Med Phys 2015;42:7090–7. https://doi.org/10.1118/1.4935865.

[9] Lehrack S, Assmann W, Bertrand D, Henrotin S, Herault J, Heymans V, et al. Submillimeter ionoacoustic range determination for protons in water at a clinical synchrocyclotron. Phys Med Biol 2017;62:L20–30.

[10] He Y. Rapid thermal conductivity measurement with a hot disk sensor: Part 1. Theoretical considerations. *Thermochim Acta* 2005;436(1):122–9. https://doi.org/10.1016/j.tca.2005.06.026.

[11] Duck F. Physical Properties of Tissue. Academic Press; 1990.

[12] Patch SK, Santiago-Gonzalez D, Mustapha B. Thermoacoustic range verification in the presence of acoustic heterogeneity and soundspeed errors – Robustness relative to ultrasound image of underlying anatomy. Med Phys 2019;46:318–27. https://doi.org/10.1002/mp.13256.

[13] John F. Duhamel's principle and the general Cauchy problem. In: Partial Differential Equations. Springer; 1981. p. 135–8.

[14] Souris K, Lee JA, Sterpin E. Fast multipurpose Monte Carlo simulation for proton therapy using multi- and many-core CPU architectures. Med Phys 2016;43:1700–12. https://doi.org/10.1118/1.4943377.

[15] Huang S, Kang M, Souris K, Ainsley C, Solberg TD, McDonough JE, et al. Validation and clinical implementation of an accurate Monte Carlo code for pencil beam scanning proton therapy. J Appl Clin Med Phys 2018;19:558–72. https://doi.org/10.1002/acm2.12420.

[16] Treeby BE, Cox BT. k-Wave: MATLAB toolbox for the simulation and reconstruction of photoacoustic wave-fields. J Biomed Opt 2010;15:021314. https://doi.org/10.1117/1.3360308.

[17] Patch SK, Hoff DEM, Webb TB, Sobotka LG, Zhao T. Two-stage ionoacoustic range verification leveraging Monte Carlo and acoustic simulations to stably account for tissue inhomogeneity and accelerator-specific time structure – A simulation study. Med Phys 2018;45:783–93. https://doi.org/10.1002/mp.12681.

[18] Anastasio M, Zhang J, Modgil D, La Rivière PJ. Application of inverse source concepts to photoacoustic tomography. Inverse Prob 2007;23:S21–36. https://doi.org/10.1088/0266-5611/23/6/S03.

[19] Assmann W, Kellnberger S, Reinhardt S, Lehrack S, Edlich A, Thirolf PG, et al. Ionoacoustic characterization of the proton Bragg peak with submillimeter accuracy. Med Phys 2015;42:567–74. https://doi.org/10.1118/1.4905047.